Photodetachment of Li^- from the Li 3*s* threshold to the Li 6*s* threshold

Cheng Pan and Anthony F. Starace
Department of Physics and Astronomy, The University of Nebraska, Lincoln, Nebraska 68588-0111

Chris H. Greene
Department of Physics and Joint Institute for Laboratory Astrophysics, The University of Colorado, Boulder, Colorado 80309-0440

(Received 18 July 1995)

Eigenchannel *R*-matrix calculations (including effects of long-range multipole interactions beyond the reaction volume) for Li^- photodetachment partial cross sections from the vicinity of the Li 3*s* threshold to the Li 6*s* threshold (3.8 eV $\leqslant \hbar\omega \leqslant$ 5.65 eV) are presented. Excellent agreement with the relative total cross section measurements of U. Berzinsh *et al.* [Phys. Rev. Lett. **74**, 4795 (1995)] in the vicinity of the Li 3*s* and Li 3*p* thresholds is found. The calculated resonance structures are analyzed in detail. In particular, the energy region between the Li 4*s* and Li 5*p* thresholds (for which there are as yet no experimental measurements) is shown to have types of doubly excited resonances which are prominent only because of the nonhydrogenic Li^+ core; such types are weak or absent in higher-energy regions as well as in H^- photodetachment spectra.

PACS number(s): 32.80.Gc, 32.80.Fb, 31.15.Ar, 31.25.Jf

I. INTRODUCTION

Recent experimental measurements of doubly excited-state spectra of H^- [1] and He [2] in the vicinity of high-energy detachment or ionization thresholds [i.e., near the H(n) and $He^+(n)$ thresholds, where $n>2$] have provided theorists with a fertile set of data for elucidating propensity rules for populating particular channels [3,4]. Theory has even been able to interpret some rather weak features [5]. As we have shown [6], the experimental and theoretical work carried out for these fundamental two-electron systems serves as a useful guide for interpreting doubly excited-state spectra of the Li^- four-electron system. However, the Li^- spectra exhibit qualitatively new features not present in H^- [6].

We report here a detailed theoretical study of highly excited-state spectra for photodetachment of the Li^- negative ion. In this paper we examine the energy range from just below the Li 3*s* threshold to just below the Li 6*s* threshold. We find that the nonhydrogenic core leads to increased prominence of doubly excited states that are only very weakly populated in detachment of H^-. Also, the nondegeneracy of the Li *nl* excited-state thresholds for different orbital angular momenta *l* changes the nature of the resonance spectrum. It also permits a much more detailed experimental comparison with theoretical partial cross section results than do the corresponding degenerate H *nl* thresholds, for which an experimental energy analysis can typically only measure the sum of all partial cross sections contributing to a particular H(n) threshold.

Section II describes our theoretical approach, the eigenchannel *R*-matrix method [7,8]. Emphasis is placed on the extensions we have made to the method in order to treat highly excited Li^- photodetachment spectra (such as, e.g., our treatment of long-range multipole interactions outside the *R*-matrix box). Section III presents our calculated partial and total Li^- photodetachment cross sections over an energy region from just below the Li 3*s* threshold up to the Li 6*s* threshold. For energies in the region of the 3*s* and 3*p* thresholds, we compare our results with recent experimental measurements and a theoretical calculation [9]. We find that the key features in this region have an intimate connection with the 3*s*3*p* doubly excited state. Below the Li 5*s* and Li 6*s* thresholds we have already shown that comparison with H^- photodetachment spectra is useful for elucidating the underlying physics [6]. We present other such comparisons here (including, e.g., density plots for key doubly excited-state wave functions in various alternative coordinate representations).

II. THEORY

We focus attention in this section on those aspects of our theoretical approach that either go beyond previous work or that are specific to our calculation for Li^- (and H^- [6]) photodetachment partial cross sections. Thus we give only a very brief overview of the eigenchannel *R*-matrix method, and we present only those equations needed to define our basis states and to calculate specific partial cross sections. We explain also the model potential used to calculate our basis states inside the *R*-matrix box, and develop in more detail the close-coupling approach used to treat the important long-range interactions outside the *R*-matrix box. In addition, the key numerical aspects of our calculations are summarized.

A. Overview

The eigenchannel *R*-matrix method [7,8] aims to determine variationally a set of normal logarithmic derivatives of a system's wave function that are constant across a reaction surface *S* enclosing a reaction volume *V*. For treatments of two-electron excitations, the reaction volume *V* is that part of six-dimensional configuration space for which both electrons lie within a sphere of radius r_0. The reaction surface *S* is the set of points for which $\max(r_1,r_2)=r_0$, where r_1 and r_2 are the electron distances from the nucleus. In practice, for each range of excitation energy, r_0 is chosen to be sufficiently large that the probability of both electrons being outside r_0 is negligible. The complicated many-electron interactions

within V are treated by bound-state, configuration interaction techniques using independent electron functions and LS coupling. In most previous eigenchannel calculations, r_0 has also been chosen large enough so that long-range interaction effects are negligible. For H^-, the degeneracy of final-state H atom levels does not permit this. In the work of Sadeghpour *et al.* [4(c)] and Sadeghpour and Cavagnero [4(d)], such effects were treated analytically within the dipole representation [10,11]. In this paper, all long-range multipole interactions were treated numerically by close-coupling procedures. This permitted much smaller values of r_0 to be used than would otherwise be the case: 80 a.u. for spectra below the $n=5$ threshold and 100 a.u. for spectra below the $n=6$ threshold. [These box sizes are large enough, nevertheless, to ensure that the H($n=5$) and H($n=6$) energy manifolds in our H^- photodetachment calculations [6] are degenerate to within a fraction of 1 meV.]

B. Treatment of interactions inside the *R*-matrix sphere

Our treatment of the region inside the R-matrix sphere has been described in detail elsewhere [8] and hence will only be sketched briefly. The Li^- valence electrons are assumed to move in the following potential describing the Li^+ core [12]:

$$V(r)=\frac{-1}{r}[Z_c+(Z-Z_c)e^{-a_1 r}+a_2 r e^{-a_3 r}] - \frac{\alpha_c}{2r^4}(1-e^{-(r/r_c)^3})^2. \tag{1}$$

For our Li^- calculation, the nuclear charge is $Z=3$, and the charge of the Li^+ core is $Z_c=1$. The polarizability of the Li^+ ion is taken to be $\alpha_c=0.1894$ a.u [13]. The empirical parameters (a_1,a_2,a_3,r_c) are fitted using a least-squares method to reproduce the experimentally measured energy levels of the Li atom [14]. A set of one-electron radial wave functions $u_{nl}(r)$ are generated in the R-matrix sphere $r\leqslant r_0$ as eigenfunctions of a radial Hamiltonian including this core potential. For each l value, a number of functions which are nonzero at $r=r_0$ are also calculated.

The wave function of the system inside the reaction volume can be expanded in the form

$$\Psi=\mathscr{A}(r_1 r_2)^{-1}\sum_{n_1,l_1,n_2,l_2} c_{n_1 l_1 n_2 l_2} \times u_{n_1 l_1}(r_1)u_{n_2 l_2}(r_2)Y_{l_1 l_2 LM}(\hat{\mathbf{r}}_1,\hat{\mathbf{r}}_2), \tag{2}$$

where $\mathscr{A}$ is the antisymmetrization operator and $Y_{l_1 l_2 LM}$ is a coupled spherical harmonic function. Note that the spin part of the wave function is not given explicitly in Eq. (2) because calculations involving spin can be done separately in the LS coupling scheme used in this work. For the bound initial state Ψ_0, $L=M=0$, and the wave function is zero for $r_1\geqslant r_0$ or $r_2\geqslant r_0$. For the final state, $L=1$, and the expansion contains terms having nonzero $u_{n_2 l_2}(r_0)$ for all the N channels assumed to have nonzero wave functions outside the reaction volume. These include N_o channels which are open at a given total energy E for the system. These channels can be specified by the quantum numbers $\{n_1,l_1,l_2\}$, where n_1 and l_1 specify the inner electron and l_2 specifies the outer electron.

The eigenchannel R-matrix method gives a set of solutions Ψ_β $(\beta=1,\ldots,N)$. If we denote $\{n_1,l_1,l_2\}$ by i, denote $r_1^{-1}u_{n_1 l_1}Y_{l_1 l_2 LM}$ by ϕ_i, and sum Eq. (2) over n_2, these solutions can be written as

$$\Psi_\beta=\mathscr{A}r_2^{-1}\sum_{i=1}^{N}\phi_i(\mathbf{r}_1,\hat{\mathbf{r}}_2)F_{i\beta}(r_2), \tag{3}$$

where $r_2=r_0$, and where $F_{i\beta}$ is defined by comparison of Eqs. (2) and (3), using the definitions just given.

C. Treatment of interactions outside the *R*-matrix sphere

Outside the reaction volume, a base set of multichannel wave functions denoted by index μ can be expressed as

$$\Psi_\mu=\mathscr{A}r_2^{-1}\sum_{i=1}^{N}\phi_i(\mathbf{r}_1,\hat{\mathbf{r}}_2)G_{i\mu}(r_2), \quad r_2\geqslant r_0. \tag{4}$$

For each μ, the radial functions $G_{i\mu}(r)$ satisfy the coupled equations

$$\left(-\frac{1}{2}\frac{d^2}{dr^2}+\frac{l_{2i}(l_{2i}+1)}{2r^2}+V(r)-(E-\epsilon_{1i})\right)G_{i\mu}(r) + \sum_{j=1}^{N}\sum_{\lambda}\frac{d_{ij}^{\lambda}}{r^{\lambda+1}}G_{j\mu}(r)=0, \tag{5}$$

where ϵ_{1i} is the energy of the inner electron in the ith channel. In Eq. (5) d_{ij}^{λ} denotes the multipole moment,

$$d_{ij}^{\lambda}=\langle\phi_i(\mathbf{r}_1,\hat{\mathbf{r}}_2)|r_1^{\lambda}P_\lambda[\cos(\hat{\mathbf{r}}_1\cdot\hat{\mathbf{r}}_2)]|\phi_j(\mathbf{r}_1,\hat{\mathbf{r}}_2)\rangle, \tag{6}$$

where P_λ is the λth Legendre polynomial. These long-range multipole terms stem from the direct part of the Coulomb interaction between the detached electron and the atomic electrons.

The index μ is defined by specifying the asymptotic boundary conditions satisfied by the radial functions $G_{j\mu}$. A set of linearly independent wave functions Ψ_μ can be obtained, for example, by requiring [15]

$$G_{j\mu}(r)\xrightarrow{r\to\infty}\begin{cases}-i(2\pi k_j)^{-1/2}e^{i(k_j r-l_{2j}\pi/2)}\delta_{j\mu}, & 1\leqslant\mu\leqslant N_o\\ -i(2\pi k_j)^{-1/2}e^{-i(k_j r-l_{2j}\pi/2)}\delta_{j(\mu-N_o)}, & N_o+1\leqslant\mu\leqslant 2N_o\\ e^{-\kappa_j r}\delta_{j(\mu-N_o)}, & 2N_o+1\leqslant\mu\leqslant N_o+N\end{cases} \tag{7}$$

where $k_j=[2(E-\epsilon_{1j})]^{1/2}$ $(j\leq N_o)$ and $\kappa_j=[-2(E-\epsilon_{1j})]^{1/2}$ $(j>N_o)$. The first two lines in Eq. (7) correspond, respectively, to outgoing and incoming waves in the N_o open channels; the third line corresponds to decaying exponentials in the closed channels. These asymptotic boundary conditions assume implicitly that the long-range multipole terms in Eq. (5) may be ignored for $r\rightarrow\infty$.

D. Boundary conditions and partial cross section formulas

Having defined in the previous two subsections the base functions both inside and outside the R-matrix sphere, we must now form those linear combinations of these base functions which describe asymptotically the experimentally observable channels i. Outside the reaction volume, the wave function for each open channel i satisfying the incoming-wave boundary condition is a linear combination of the Ψ_μ $(1\leq\mu\leq N_o+N)$,

$$\Psi_i^{(-)}=\sum_{\mu=1}^{N_o}\Psi_\mu\delta_{\mu i}-\sum_{\mu=1}^{N}\Psi_{N_o+\mu}a_{\mu i}. \tag{8}$$

In Eq. (8), those $a_{\mu i}$ coefficients for wave functions containing incoming-wave components (i.e., for $1\leq\mu\leq N_o$) give the elements of the scattering matrix $S^\dagger$,

$$S^\dagger_{ij}=a_{ij}, \quad i,j=1,\ldots,N_o. \tag{9}$$

Inside the reaction volume, $\Psi_i^{(-)}$ can be obtained as a linear combination of the eigenchannel wave functions,

$$\Psi_i^{(-)}=\sum_{\beta=1}^{N}\Psi_\beta b_{\beta i}. \tag{10}$$

Matching of Eqs. (8) and (10) at $r_2=r_0$ leads to the following simultaneous system of equations:

$$\sum_{\beta=1}^{N}F_{j\beta}(r_0)b_{\beta i}+\sum_{\mu=1}^{N}G_{j(N_o+\mu)}(r_0)a_{\mu i}=G_{ji}(r_0) \quad (1\leq j\leq N), \tag{11}$$

$$\sum_{\beta=1}^{N}F'_{j\beta}(r_0)b_{\beta i}+\sum_{\mu=1}^{N}G'_{j(N_o+\mu)}(r_0)a_{\mu i}=G'_{ji}(r_0) \quad (1\leq j\leq N). \tag{12}$$

Each open channel i has a different set of inhomogeneous terms on the right hand sides of Eqs. (11) and (12). Thus for each i the $2N$ equations with $2N$ unknown coefficients $b_{\beta i}$ and $a_{\mu i}$ have a unique solution.

Once the coefficients defining the states $\Psi_i^{(-)}$ corresponding to the experimentally observable channels i are determined, the partial cross sections may be calculated according to the standard formula [16]:

$$\sigma_i=\frac{4\pi^2\omega}{c}|\langle\Psi_i^{(-)}|D|\Psi_0\rangle|^2, \tag{13}$$

where c is the speed of light, ω is the photon energy, and D is the dipole operator. For light linearly polarized along $\hat{\mathbf{z}}$, the length form of the dipole operator is defined as $D_L=z_1+z_2$, and the velocity form is defined as $D_V=-i(d/dz_1+d/dz_2)/\omega$.

E. Numerical aspects of the calculation

We present here a few of the numerical details of our calculations in order that the reader may better judge the reliability of our results. Inside the R-matrix sphere, 38 closed-type (i.e., zero at $r=r_0$) and two open-type (i.e., nonzero at $r=r_0$) one-electron radial wave functions are evaluated for each of the orbital angular momenta $0\leq l\leq 6$. We include 794 closed-type, two-electron configurations (denoted by n_1l_1,n_2l_2) in the R-matrix calculation. These are zero outside the R-matrix sphere. For each channel in which an electron can escape from the reaction volume, we include two open-type orbitals for the outer electron in addition to the closed-type basis set. For a given photon energy, if n denotes the highest n_1 value among all the open channels at this energy, then all the $\{(n+2),l_1,l_2\}$ channels with $n+2<8$ and $l_1,l_2<7$ are treated as having nonzero wave functions outside the R-matrix sphere and are included in the calculation. That is to say, for the highest photon energy considered, all of the 47 channels described by $2\leq n_1\leq 7$ and $0\leq l_1,l_2\leq 6$ are included.

The asymptotic boundary conditions given in Eq. (7) are, of course, not exactly satisfied at any finite distance from the nucleus. For this reason, in practice we use WKB representations for the wave functions instead of the expressions in Eq. (7). More specifically, for one-electron continuum wave functions outside the R-matrix box, values calculated using a WKB method [17,18] at a suitably large distance are used as boundary conditions to replace the first two expressions in Eq. (7). When needed, they are numerically integrated inward to the point at which we start to integrate Eq. (5). For weakly closed channel wave functions outside the R-matrix box, WKB boundary conditions [19] are used in place of the last expression in Eq. (7)

Equation (5) is solved using Numerov's method [20]. For a given photon energy, it is solved up to a distance at which the smallest kinetic energy among those of the continuum electrons in all open channels can be considered large as compared to the largest long-range term in Eq. (5). However, for all the photon energies considered in this calculation, a cutoff for the distance is chosen to be 1000 a.u. Finally, multipole moments up to $\lambda=3$ (octal moments) are included in Eq. (5).

III. RESULTS

This section groups our total and partial cross section results according to the photon energy, as this is generally most useful for experimentalists. We defer to another presentation our consideration of the region between the lowest detachment threshold (Li $2s$) and the Li $3s$ threshold, since comparisons with the numerous experimental and theoretical studies in this region would greatly enlarge the present paper. By contrast, the energy region above the Li $3s$ threshold is almost unexplored. Aside from our theoretical results, experiments between the $3s$ and $3p$ thresholds have only recently been carried out [9]. Also, we have recently learned of a theoretical calculation (using a discrete basis set, complex

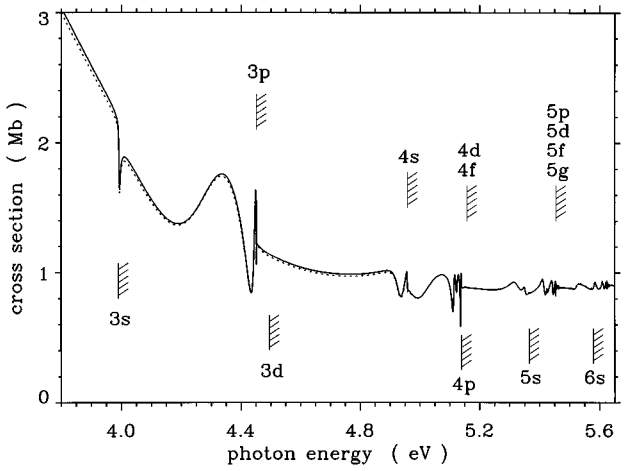

FIG. 1. Calculated total photodetachment cross section for Li^- for photon energies from 3.8 eV to 5.65 eV. Full (dotted) curves give dipole velocity (length) results. The Li(nl) thresholds in this energy region are indicated.

rotation method) for the total photodetachment cross section of Li^- up to the Li(4d) threshold [21]. The spectra above the Li ns thresholds for $n \geq 3$ show many common features; they also display revealing similarities to and differences from the corresponding spectra for H^-.

An overview of our results is shown in Fig. 1. This figure presents the total photodetachment cross section for Li^- over the photon energy range 3.8 eV $\leq \hbar w \leq$ 5.65 eV, which encompasses the energy region from just below the Li 3s threshold to just below the Li 6s threshold. The lowest ns and np thresholds for $n=3-5$ are marked. We examine each of the ns and np threshold regions in turn. A preliminary report of some of this work has been presented elsewhere [22].

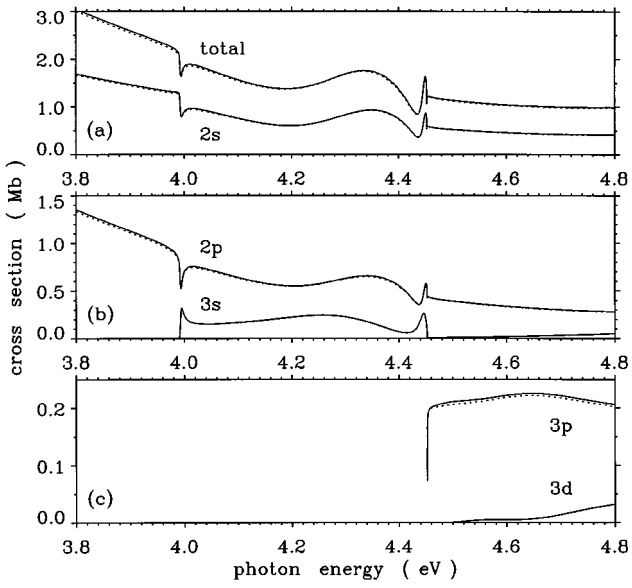

FIG. 2. Calculated total (σ_T) and partial [$\sigma(nl)$] photodetachment cross sections for Li^- for photon energies 3.8 eV $\leq \hbar\omega \leq$ 4.8 eV. Full (dotted) curves give dipole velocity (length) results. (a) σ_T and $\sigma(2s)$. (b) $\sigma(2p)$ and $\sigma(3s)$. (c) $\sigma(3p)$ and $\sigma(3d)$.

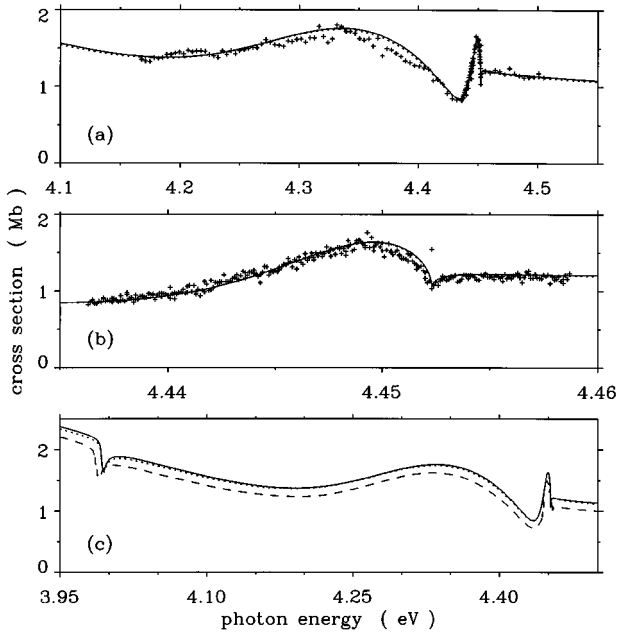

FIG. 3. Comparison of our calculated total photodetachment cross sections in dipole velocity (solid curve) and dipole length (dotted curve) approximation with results of Ref. [9]. Relative experimental results [9] are normalized to our theoretical velocity curve at $\hbar\omega = 4.45$ eV. (a) Comparison with experimental results (+) of Ref. [9] over the energy range $4.1 \leq \hbar\omega \leq 4.55$ eV. (b) Comparison with experimental results (+) of Ref. [9] in the vicinity of the Li(3p) threshold. (c) Comparison with theoretical results (dashed curve) of Lindroth [9,21].

A. Li^- photodetachment near the Li 3s and 3p thresholds

In Figs. 2 and 3 we present our results for the partial photodetachment cross sections $\sigma(nl)$ for the processes

$$Li^- + \gamma \rightarrow Li(nl) + e^-, \tag{14}$$

as well as for the total detachment cross section, $\sigma_T = \Sigma_{nl}\sigma(nl)$, in the vicinity of the Li 3s and 3p thresholds. Figure 2 presents σ_T and the partial cross sections for $nl = 2s, 2p, 3s, 3p$, and $3d$.

Since the ground-state term level of Li^- is $^1S^e$, electric dipole selection rules in LS coupling imply that only $^1P^o$ final-states can be reached. This in turn implies that for $nl = ns$, the partial cross section $\sigma(ns)$ corresponds to the single final-state channel Li $ns\epsilon p\ ^1P^o$. However, in general $\sigma(nl)$ for $l > 0$ is a sum of the partial cross sections for at least two final-state channels, Li $nl\epsilon(l \pm 1)\ ^1P^o$, and possibly others. Thus, e.g., $\sigma(2p)$ in Fig. 2(b) is the sum of the partial cross sections for the $2p\epsilon s\ ^1P^o$ and $2p\epsilon d\ ^1P^o$ channels.

There appears at first glance to be little resemblance between the Li^- photodetachment cross section in the vicinity of the 3s and 3p thresholds and the corresponding H^- photodetachment cross section near the $n=3$ threshold. As was found both experimentally [23] and theoretically [4(c)], the H^- photodetachment cross section below the $n=3$ threshold is marked by a broad window resonance of the type ${}_3\{0\}_3^+$. [We employ here the notation ${}_N\{v\}_n^A$ introduced in Ref. [4]. Here v is the vibrational quantum number, indicat-

TABLE I. $^1P^o$ autoionizing levels of Li^- below the Li $3p$ threshold.

Authors	Ref.	Method	Resonance energy (a.u.)[a]	Li^- (^1S) ground-state energy (a.u.)[a]	Photon energy (eV)[b]
Fung and Matese	[28]	projection	−0.0575	−0.218 85	4.39
Stewart *et al.*	[29]	projection	−0.0594	−0.219 98	4.37
		stabilization	−0.0587	−0.219 98	4.39
Lin	[30]	diabatic hyperspherical	−0.0671	−0.220 87	4.18
Lindroth	[9,21]	discrete basis/ complex rotation	−0.0620	−0.220 87	4.32
Present work		projection (excluding $3s3p$)	−0.059 61	−0.220 85	4.39
		projection (including $3s3p$)	−0.065 71	−0.220 85	4.22
			−0.057 86[c]	−0.220 85	4.44

[a]Below the Li^+ ground-state threshold.
[b]Above the Li^- (^1S) ground state using the conversion 1 a.u. = 27.2114 eV.
[c]This is a second $^1P^o$ autoionizing resonance.

ing the number of nodes in θ_{12} (in the hyperspherical representation) or in λ (in the prolate spheroidal coordinate representation); A indicates the possible symmetry of the wave function with respect to $r_1=r_2$, with $A=+$ indicating an antinode at $r_1=r_2$ and $A=-$ indicating a node at $r_1=r_2$; finally $N(n)$ is the principal quantum number of the lower-(higher-) energy member of the doubly excited electron pair.] Theory [4(c),24–27] predicts also a very narrow Feshbach resonance of the type ${}_3\{0\}_4^-$, which has not been observed [23]. Just below the $n=3$ threshold, higher members of these $+$ and $-$ channels are predicted [24–27,4(c)]; the ${}_3\{0\}_4^+$ resonance has been observed [23]. Despite the lack of similarity between the H^- and Li^- photodetachment spectra in this energy region, due most likely to the lack of degeneracy of the Li $3s$ and Li $3p$ thresholds, the search for resonances of the $+$ and $-$ type will prove useful for interpreting our Li^- detachment results, as we discuss below.

Our total cross section results for Li^- are in excellent agreement with recent relative measurements near the Li $3p$ threshold [9], as shown in Fig. 3. Both on the broad energy scale shown in Fig. 3(a) and on the fine energy scale shown in Fig. 3(b) (near the $3p$ threshold), our calculated total detachment cross section, which predated the measurements (cf. Ref. [22]), shows a very accurate prediction of experimentally observed features. Furthermore, Fig. 3(c) compares our total cross section results with those of Lindroth [21]; there is excellent qualitative agreement, although our results lie ≈5–10 % higher in this energy region. Hence the lack of an obvious similarity between the H^- and Li^- photodetachment cross sections near the $n=3$ thresholds does not imply any inaccuracy in the present calculations, but rather highlights features in the Li^- photodetachment cross section (such as the broad minimum and subsequent maximum near 4.2 eV and 4.35 eV, respectively, as well as the sharper minimum and subsequent maximum just below the $3p$ threshold) that require interpretation.

Prior theoretical studies of Li^- doubly excited-state resonances below the $3p$ threshold predict only a single $^1P^o$ resonance [28–30]. These predictions are summarized in Table I. Fung and Matese [28] and Stewart *et al.* [29] used a Feshbach projection operator technique to locate $^1P^o$ autoionizing resonances for Li^- below the Li $3p$ threshold. According to this technique, all one-electron orbitals with energies below the $3p$ level were excluded in the configuration interaction calculation since such orbitals serve to represent continuum channels that are open below the $3p$ threshold. Hence all bound orbitals $1s$, $2s$, $2p$, and $3s$ were excluded from the multiconfiguration calculation. Both works [28,29] predict a single $^1P^o$ autoionizing level located at −0.058 or −0.059 a.u. relative to the Li^+ threshold. (See Table I for the corresponding photon energies.) Lindroth [9,21] has performed a discrete basis set, complex rotation calculation that finds a resonance at −0.062 a.u., somewhat below the energies predicted by Refs. [28,29]. Lin [30] carried out a diabatic hyperspherical calculation for the $^1P^o$ potential converging to the Li $3p$ threshold. He found that this potential supports a bound state (which he labeled "$3s$ $3p$") at an energy of −0.0671 a.u., which is quite a bit below the resonance energy for this state predicted by Refs. [28,29]. (In contrast, for other symmetries Lin's predicted resonance energies are in quite good agreement with those of Refs. [28,29].)

Table I also presents our projection operator results for doubly excited-state energies obtained by two different methods. The first method excluded all one-electron orbitals below $3p$. The result was a single resonance below the $3p$ threshold located at −0.059 61, which is in excellent agreement with the similar result of Stewart *et al.* [29]. We then carried out a nonstandard projection operator calculation in which all configurations having orbitals lower in energy than $3p$ are excluded *except* for the configuration $3s3p$, which is included. The result is that we obtained two resonances below the $3p$ threshold, at −0.065 71 a.u. and −0.057 86 a.u. We note that the lowest of these is very close in energy to the diabatic hyperspherical "$3s3p$" resonance predicted by Lin at −0.0671 a.u.

Figure 4 shows density plots of the three resonance states we calculated as just described. The resonance at −0.059 61 a.u., obtained by excluding $3s3p$ from the calculation, is not a so-called ridge-riding state (in which both electrons are

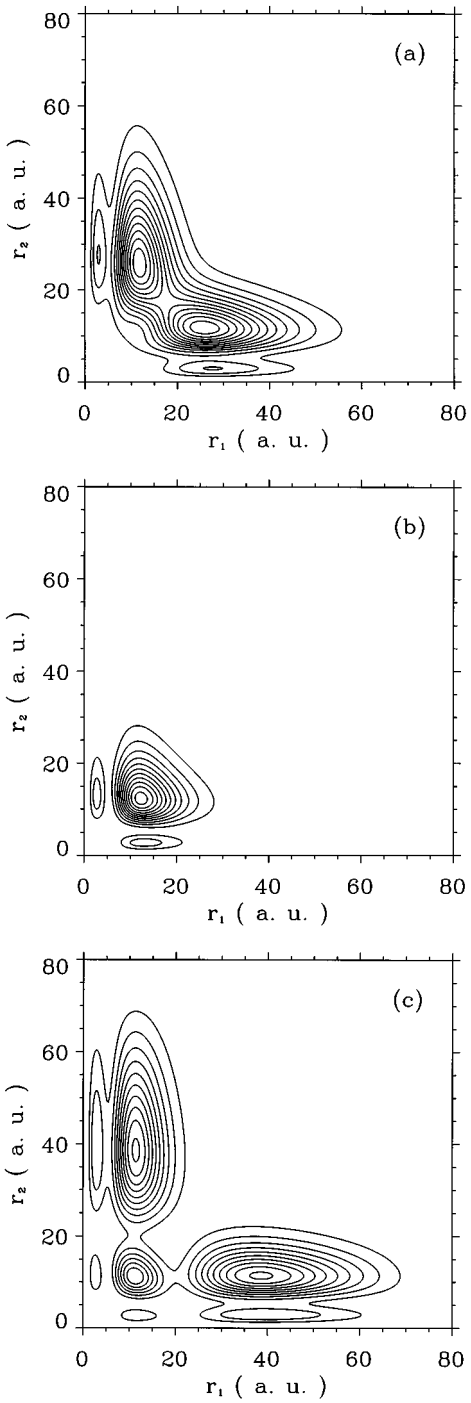

FIG. 4. Probability density plots for the $^1P^o$ two-electron discrete states between the Li(3s) and Li(3p) thresholds, whose energies are given in Table I. These states are calculated as described in the text. Probability densities are integrated over angular variables $(\hat{r}_1,\hat{r}_2)$, and plotted vs (r_1,r_2). (a) Resonance at $-0.059\,61$ a.u. (b) Resonance at $-0.065\,71$ a.u. (c) Resonance at $-0.057\,86$ a.u.

predominantly at equal distances from the nucleus). On the other hand, the lowest resonance obtained by including the $3s3p$ configuration *is* such a ridge-riding state with a strong $+$ character. The $+$ character of this resonance is the major point of similarity to the H^- photodetachment spectrum in the vicinity of the $n=3$ threshold. Whereas this lowest resonance obtained by including the $3s3p$ configuration appears

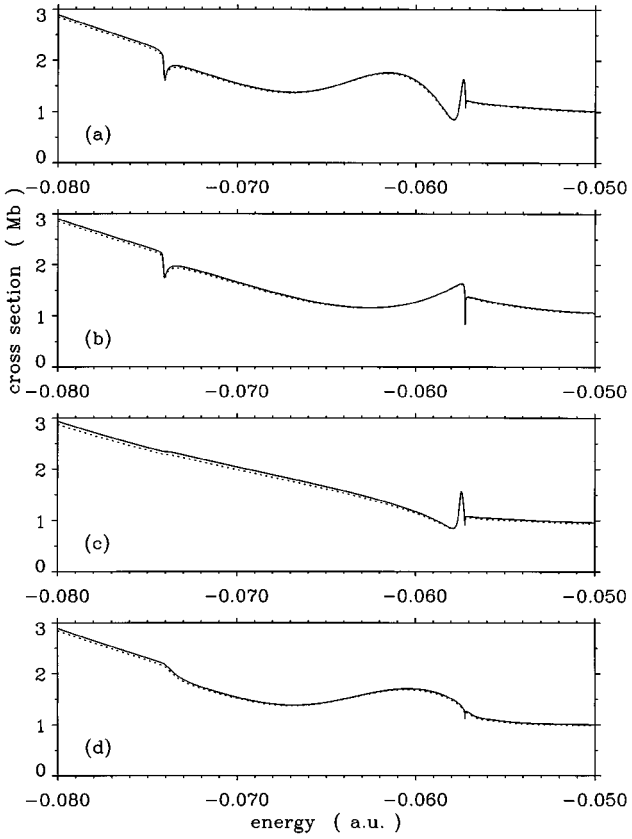

FIG. 5. Effects of resonances on the calculated total photodetachment cross section for Li^- in the vicinity of the Li(3s) and Li(3p) thresholds plotted vs energy (in a.u.) below the Li^+ threshold. Background cross sections corresponding to each of the three resonances described in the text (having energies listed in Table I) are obtained using the isolated resonance theory of Ref. [31]. Dipole velocity (length) results are given by the solid (dotted) curves. (a) σ_T. (b) Background cross section for the $-0.059\,61$ a.u. resonance at $\hbar\omega=4.39$ eV. (c) Background cross section for the -0.6571 a.u. resonance at $\hbar\omega=4.22$ eV. (d) Background cross section for the $-0.057\,86$ a.u. resonance at $\hbar\omega=4.44$ eV.

to have little overlap with continuum channels, the second resonance state we obtain does appear to have significant overlap (since its probability amplitude is primarily located at large distances along the axes in Fig. 4). This second resonance does not have any obvious $+$ or $-$ character.

In order to determine the effect of the three resonances whose densities are shown in Fig. 4 on the Li^- photodetachment cross sections, we have used the isolated resonance theory [31] to remove the effect of each of these resonances on the cross section. The results are shown in Fig. 5. Figure 5(a) shows the total cross section and Figs. 5(b), 5(c), and 5(d) show the ''background'' cross sections that result from removing the resonances at $-0.059\,61$ a.u., $-0.065\,71$ a.u., and $-0.057\,86$ a.u., respectively, that we have calculated as described above. Figure 5(b) shows that the resonance we calculate at $-0.059\,61$ a.u. using the standard projection operator method (i.e., excluding the $3s3p$ configuration) is responsible for the broad maximum in the cross section located in the vicinity of -0.060 a.u. The results of our nonstandard projection operator calculation (i.e., including the $3s3p$ configuration) are more interesting. As shown in Fig. 5(c), the

lowest resonance appears to be responsible for nearly all of the structure in the photodetachment cross section from the $3s$ threshold to just below the $3p$ threshold. The second resonance we calculate by our nonstandard method appears to be responsible for the sharp maximum observed just below the $3p$ threshold, as shown in Fig. 5(d).

With regard to the resonance results of Lindroth [9,21], she finds [9] the resonance "dominated by the configurations $3p3d$ and $4s3p$, and there appears to be no significant contributions to the localized part of the wave function from configurations with one electron in the $3s$ orbital, which is also in contrast to the case of H^-." Lindroth finds the width of the lowest resonance to be so broad that it overlaps the Li $3p$ threshold (making description of this resonance by a Fano isolated resonance profile not possible). She also finds [9] "a narrower resonance structure lies just below the $3p$ threshold." Our results using the standard projection procedure (i.e., excluding the $3s3p$ configuration) agree qualitatively with the results of Lindroth, giving a not very well-localized resonance [cf. Fig. 4(a)]. Also, when we remove the effect of this resonance on the cross section by use of the Fano resonance formula, the result is not satisfactory since the cross section still has much structure [cf. Fig. 5(b)]. However, when we include the $3s3p$ configuration in our nonstandard calculation, we do get a localized state [cf. Fig. 4(b)], as is found in Ref. [9] for H^-, and the use of the Fano profile formula to remove the effect of this resonance shows that nearly all structure is removed from the cross section [cf. Fig. 5(c)].

We hasten to state that we regard the results of our nonstandard projection operator calculation as suggestive but not definitive. In contrast to the agreement found for other symmetries, the significant discrepancy between the diabatic hyperspherical result of Lin [30] for the $^1P^o$ resonance below the $3p$ threshold and the results of the more standard configuration interaction approaches of Refs. [28,29] indicate that electron correlation effects below the Li $3p$ threshold appear to be very sensitive to the theoretical approach employed. Nevertheless, the excellent agreement that our eigenchannel R-matrix calculations have with the recent experimental measurements (cf. Fig. 3), in spite of this sensitivity, gives us confidence in our predictions at higher energies, where no experimental measurements are available.

B. Li^- photodetachment near the Li $4s$ and $4p$ thresholds

Our results in Figs. 6 and 7 show the total and partial Li^- photodetachment cross sections in the photon energy region 4.8 eV $\leqslant\hbar\omega\leqslant$5.2 eV. This energy region covers the $4s$, $4p$, $4d$, and $4f$ thresholds of excited Li (cf. Table II). In Fig. 6 we present our total and Li(ns) partial cross sections ($2\leqslant n\leqslant 4$). In Fig. 7 we present our Li(np) ($2\leqslant n\leqslant 4$) and Li($3d$) partial cross sections as well as the sum of the Li($4d$) and Li($4f$) partial cross sections.

Some observations can be made regarding these partial cross sections. First, significant resonance structure is apparent in all partial cross sections for channels that are open below the Li($4p$) threshold. Second, for fixed l, the partial cross sections Li(nl) exhibit deeper resonance windows below the Li($4p$) threshold the larger n is. Third, according to the theory for a resonance interacting with many open channels [31(b)], the depth of a window resonance in a particular partial cross section is a measure of the strength of interaction of that resonance with the channels belonging to that partial cross section. In the limit that there is only a single continuum channel interacting with the resonance, the cross section goes through zero at the minimum of the window resonance [31(a)]. The presence of more than a single open channel leading to a particular partial cross section generally results in a finite total cross section at the minimum of the window resonance [31]. However, the partial cross sections might individually go through zero [31(b)].

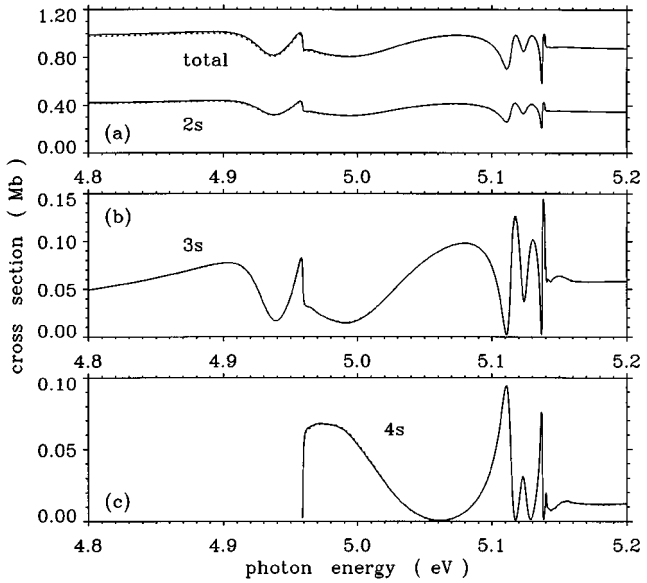

FIG. 6. Total (σ_T) and partial [$\sigma(ns)$] photodetachment cross sections for Li^- for photon energies 4.8 eV $\leqslant\hbar\omega\leqslant$ 5.2 eV. Dipole velocity (length) results are indicated by the solid (dotted) lines. (a) σ_T and $\sigma(2s)$. (b) $\sigma(3s)$. (c) $\sigma(4s)$.

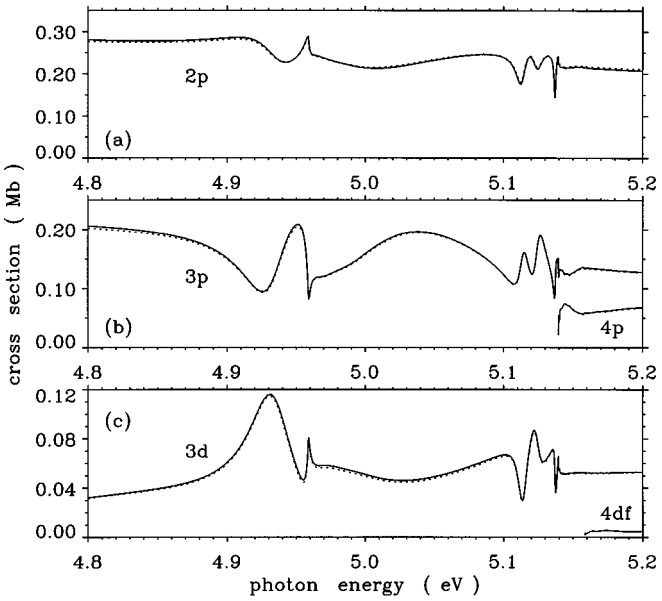

FIG. 7. Same as in Fig. 6 for $\sigma(nl)$ partial cross sections with $l>0$. (a) $\sigma(2p)$. (b) $\sigma(3p)$ and $\sigma(4p)$. (c) $\sigma(3d)$ and the sum of $\sigma(4d)$ and $\sigma(4f)$ (indicated by "$4df$").

TABLE II. Calculated Li(nl) thresholds.

Threshold	Energy (a.u.)[a]	Photon energy (eV)[b]
$3s$	−0.074 20	3.991
$3p$	−0.057 23	4.452
$3d$	−0.055 62	4.496
$4s$	−0.038 62	4.959
$4p$	−0.031 97	5.140
$4d$	−0.031 28	5.158
$4f$	−0.031 25	5.159
$5s$	−0.023 64	5.366
$5p$	−0.020 37	5.455
$5d$	−0.020 01	5.465
$5f$	−0.020 00	5.465
$5g$	−0.020 00	5.465
$6s$	−0.015 84	5.579

[a]Relative to the Li^+ ground-state threshold. Finite nuclear mass corrections are not included.

[b]Relative to the $Li^-(^1S^o)$ ground state at −0.220 85 a.u.

Applying these observations to the particular partial cross sections in Figs. 6 and 7, we note the following. The Li($2s$) and Li($2p$) partial cross sections give the largest contributions to the total detachment cross sections. However, only relatively small percentages of these partial cross sections interact with the doubly excited states below the $4p$ threshold (cf. Ref. [31(b)]). In contrast, the Li($3s$) and Li($4s$) partial cross sections are completely dominated by interactions with these doubly excited states; they exhibit very deep window resonances that in many instances plunge the partial cross sections by nearly 100%, to values close to zero. Note that only a single channel converges on these thresholds, viz., Li(ns)$\epsilon p(^1P^o)$. If there were no interactions between these channels and the other open $^1P^o$ channels, then the partial cross sections at the minima of the window resonances would be zero. That the cross section minima are indeed nearly zero within the window resonances implies that interchannel interactions are weak. Note further that the minima in the Li($3s$) and Li($4s$) partial cross sections occur at different energies within the resonance. Indeed, comparing Figs. 6(b) and 6(c), one sees that these partial cross sections are nearly mirror images of one another. This kind of behavior has been predicted in Fig. 3 of Ref. [31(b)]. We observe also that the Li($3p$) and Li($3d$) partial cross sections exhibit striking effects of resonances, but these are more subdued than for the Li($3s$) and Li($4s$) partial cross sections, i.e., the window resonances never drop the cross sections by more than about 50%.

Lindroth has calculated the total photodetachment cross section for Li^- in the vicinity of the Li($4s$) and Li($4p$) threshold [21]. Our results are in excellent qualitative agreement with hers. However, our results are about 15–20 % larger in magnitude.

C. Li^- photodetachment near the Li $5s$ and $5p$ thresholds

Our results in Figs. 8–10 show the total and partial Li^- photodetachment cross sections in the photon energy region 5.2 eV $\leqslant \hbar\omega \leqslant$ 5.5 eV. This energy region covers the $5s$, $5p$, $5d$, $5f$, and $5g$ thresholds of excited Li (cf. Table II). In Fig. 8 we present our total and Li(ns) partial cross sections ($2 \leqslant n \leqslant 5$). In Fig. 9 we present the Li(np) partial cross sections ($2 \leqslant n \leqslant 5$). Finally, in Fig. 10 we present the Li($3d$), Li($4d$), and Li($4f$) partial cross sections as well as the sum of the Li($5d$), Li($5f$), and Li($5g$) partial cross sections.

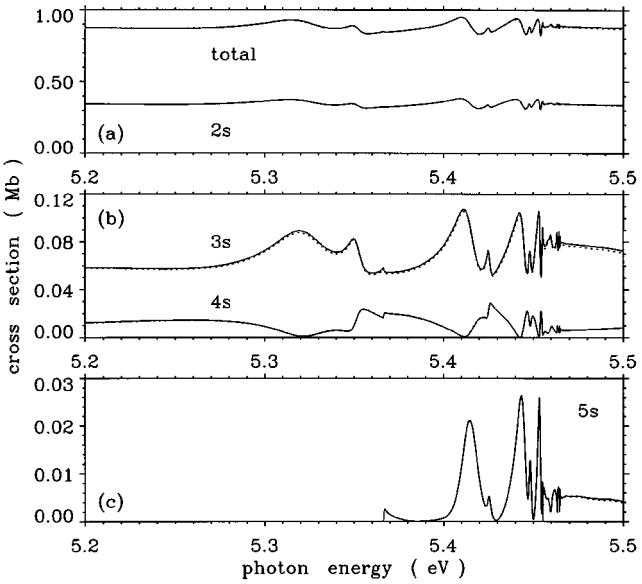

FIG. 8. Total (σ_T) and partial [$\sigma(ns)$] photodetachment cross sections for Li^- for photon energies 5.2 eV$\leqslant\hbar\omega\leqslant$5.5 eV. Dipole velocity (length) results are indicated by the solid (dotted) lines. (a) σ_T and $\sigma(2s)$. (b) $\sigma(3s)$ and $\sigma(4s)$. (c) $\sigma(5s)$.

Most of our general observations on the partial cross sections near the Li $4s$ and $4p$ thresholds, presented in Sec. III B, apply here as well. Namely, for $n=2$ and 3 the partial cross sections all have large ''background'' cross sections which do not interact significantly with the doubly excited states below the $5p$ threshold. Of these, the $3s$ partial cross

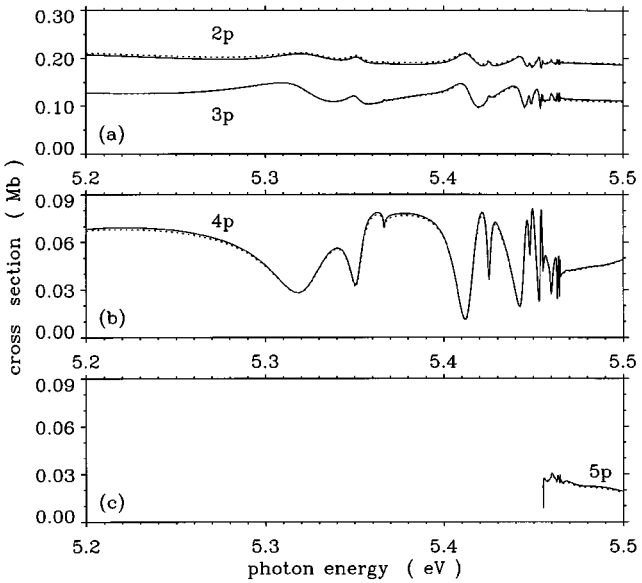

FIG. 9. Same as in Fig. 8 for $\sigma(np)$ partial cross sections. (a) $\sigma(2p)$ and $\sigma(3p)$. (b) $\sigma(4p)$. (c) $\sigma(5p)$.

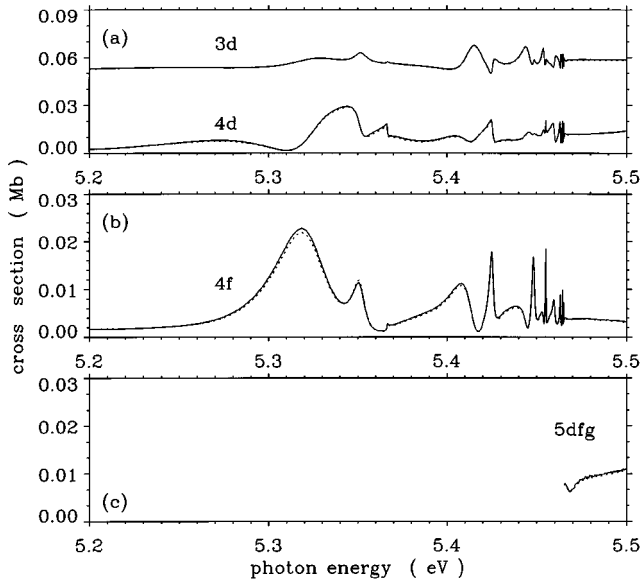

FIG. 10. Same as in Fig. 8 for $\sigma(nl)$ partial cross sections with $l>1$. (a) $\sigma(3d)$ and $\sigma(4d)$. (b) $\sigma(4f)$. (c) Sum of $\sigma(5d)$, $\sigma(5f)$, and $\sigma(5g)$ partial cross sections (indicated by "$5dfg$").

section shows the most prominent resonance structures, but these structures reduce the partial cross sections by less than 50%. In contrast, the $4s$ and $5s$ partial cross sections are completely dominated by interactions with doubly excited states, also with deep window resonances that plunge the cross sections by nearly 100%. Furthermore, the $4s$ and $5s$ partial cross sections appear to be mirror images of one another, with one having a maximum when the other has a minimum, just as we have noted for the $3s$ and $4s$ partial cross sections in Fig. 6. Only slightly less dominated by resonance structures are the $4p$, $4d$, and $4f$ partial cross sections, due most likely to a greater weighting of pd and df configurations (relative to sp configurations) in the doubly excited states below the $5p$ threshold than is the case below the $4p$ threshold. Another factor may be that while the Li($4d$) and Li($4f$) partial cross sections each have contributions from two continuum final-state $^1P^o$ channels, in practice there may be only one important final-state channel, namely, the one having the lowest allowable orbital angular momentum for the continuum electron. Hence the deep window resonances in these two partial cross sections may stem from the fact that they have contributions from effectively only a single channel.

D. Comparisons of the Li($n-1$) partial cross sections below the Li(np) thresholds

In Fig. 11 we plot the partial cross sections $\sigma(n=2),\sigma(n=3),\sigma(n=4)$, and $\sigma(n=5)$ below the corresponding Li $(n+1)p$ thresholds. These partial cross sections are the ones with the most direct similarity to the photodetachment partial cross sections of H^-, as discussed elsewhere [6]. We have plotted the partial cross sections in Fig. 11 in such a way that the Li $(n+1)p$ thresholds are roughly coincident (cf. Table II).

A key feature of the $\sigma(n)$ partial cross sections is the increasing prominence of the + type resonance that lies near 4.22 eV in the $\sigma(n=2)$ partial cross section, well above the

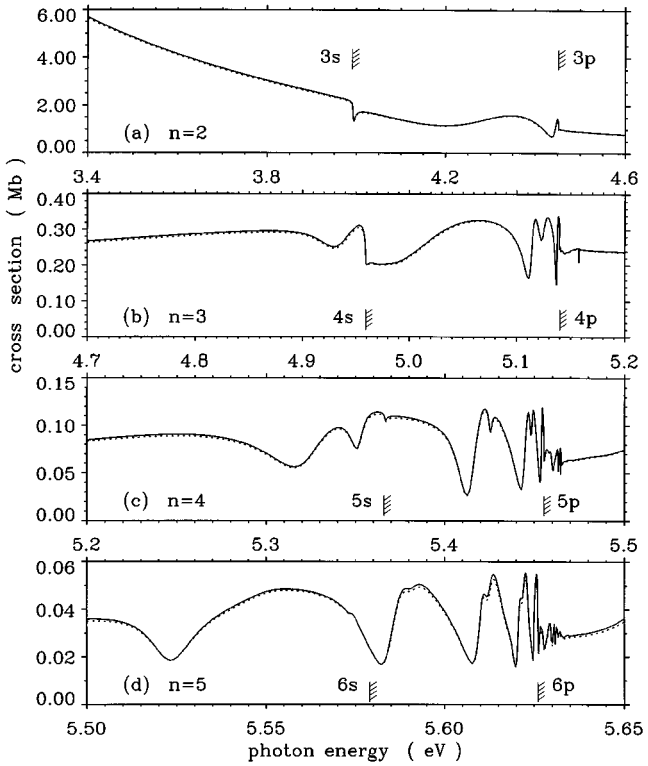

FIG. 11. Partial cross sections [$\sigma(n)$] for Li^- photodetachment below the Li($n+1$)p threshold for $2\leq n\leq 5$. (a) $\sigma(n=2)$ for 3.4 eV$\leq\hbar\omega\leq$4.6 eV. (b) $\sigma(n=3)$ for 4.7 eV$\leq\hbar\omega\leq$5.2 eV. (c) $\sigma(n=4)$ for 5.2 eV$\leq\hbar\omega\leq$5.5 eV. (d) $\sigma(n=5)$ for 5.5 eV $\leq\hbar\omega\leq$5.65 eV. The Li(ns) and Li(np) thresholds in these energy regions are indicated.

Li $3s$ threshold. For $n=3$ the corresponding + resonance appears close to the Li $4s$ threshold. For $n=4$ and $n=5$, the lowest member of the + series lies well below the Li $5s$ and Li $6s$ thresholds near 5.32 eV and 5.52 eV, respectively [6]. The + type resonances appear to increase in prominence as n increases. This is not surprising, since the effect of the Li^+ core becomes more hydrogenic for higher n, as more l values are nearly degenerate.

Whereas the + type resonance increases in prominence as n increases, the − type resonances decrease in prominence. Section III A above pointed out that it is difficult to characterize the cross section features in the $\sigma(n=2)$ partial cross section near the Li $3p$ threshold. Reference [6] discusses, however, the $n=4$ and $n=5$ partial cross sections, which show − type resonances between the deep + type resonances, e.g., near $\approx$5.35 eV, $\approx$5.425 eV, and $\approx$5.448 eV in the case of $\sigma(n=4)$ and near $\approx$ 5.54 eV, $\approx$ 5.59 eV, and $\approx$ 5.612 eV in the case of $\sigma(n=5)$. The dip near $\approx$ 5.12 eV in the $\sigma(n=3)$ partial cross section appears by analogy to be also a − type feature. Remarkably, these − type features that are so prominent for $\sigma(n=3)$ and $\sigma(n=4)$ are only very weak features of the $\sigma(n=5)$ partial cross section. We interpret this behavior on the basis of propensity rules for H^- photodetachment [3,4] that "forbid" population of − type reasonances, and the fact that the Li^+ core appears more and more like the H^+ core to excited electrons in high n levels with $l>0$.

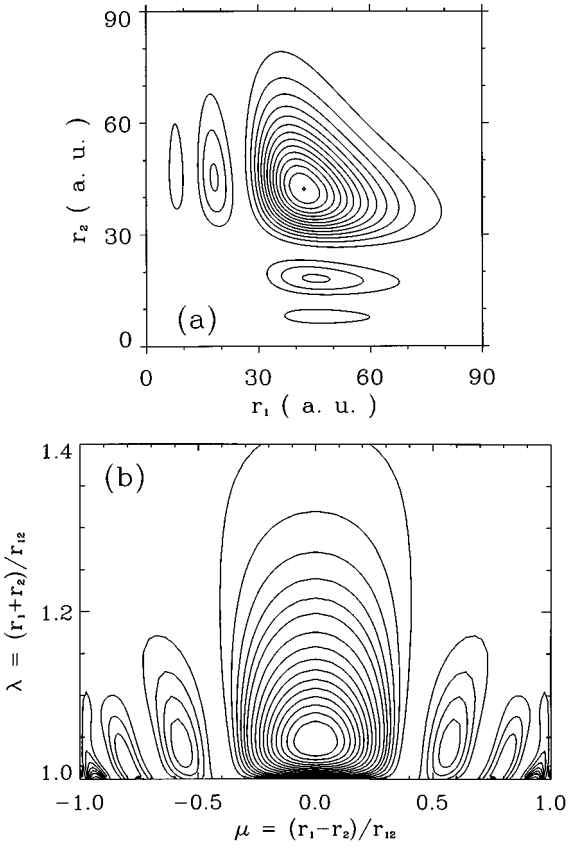

FIG. 12. Doubly excited-state ${}_5\{0\}_5^+$ wave function density plotted at its maximum value in R [i.e., $R \equiv (r_1^2+r_2^2)^{1/2}=60$ a.u.]. (a) Plotted in (r_1,r_2) coordinates. (b) Plotted in prolate spheroidal coordinates (μ,λ). Located near $\hbar\omega = 5.32$ eV in Fig. 11(c).

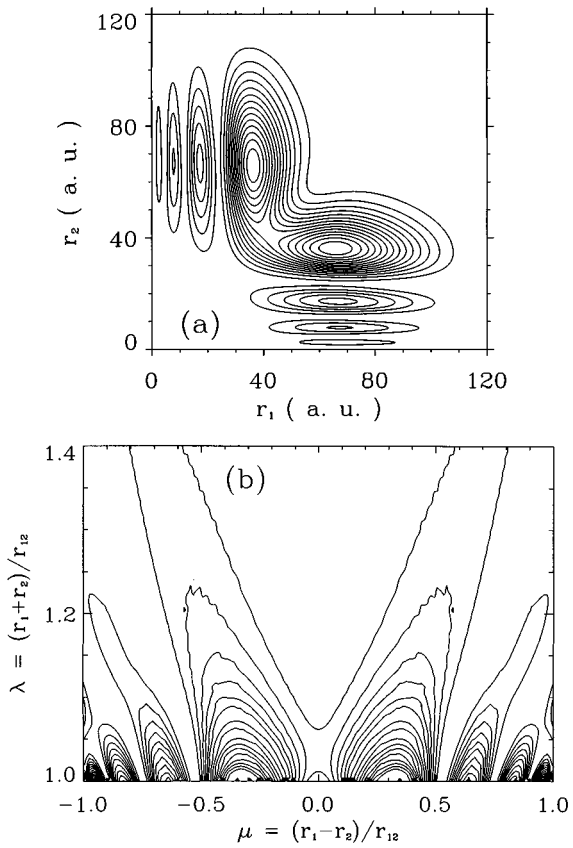

FIG. 13. Doubly excited-state ${}_5\{0\}_6^-$ wave function density plotted at its maximum value in R [i.e., $R \equiv (r_1^2+r_2^2)^{1/2}=80$ a.u.]. (a) Plotted in (r_1,r_2) coordinates. (b) Plotted in prolate spheroidal coodinates (μ,λ). Located near $\hbar\omega = 5.35$ eV in Fig. 11(c).

E. Resonance density plots

Our comments in the preceding section on the character of the resonance features in the $\sigma(n)$ partial cross sections are based on probability density plots. These are extracted from discrete resonance states derived from a separate calculation as follows: All basis functions were set to zero on the boundary of the interaction volume V. Thus only the discrete levels were calculated, in order to identify features at energies corresponding to structures in the cross sections. In Ref. [6] we presented hyperspherical coordinate density plots of three of these discrete resonances. Here we present similar density plots for the same three resonances, both in (r_1,r_2) coordinates and in prolate spheroidal coordinates μ and λ.

These density plots were made as in Ref. [6]. Briefly, special R-matrix calculations were carried out with a box size $r_0=120$ a.u. All basis functions were set to zero at the boundary. Thus only discrete structures were calculated, in order to see which ones appeared at energies corresponding to the features in the photodetachment cross sections. Each plot is made at the peak of each resonance's probability amplitude in the hyperspherical radius $R \equiv (r_1^2+r_2^2)^{1/2}$. For the (r_1,r_2) plots we have integrated the probability densities over all angles $(\hat{\mathbf{r}}_1,\hat{\mathbf{r}}_2)$.

Figure 12 shows density plots for the ${}_5\{0\}_5^+$ resonance feature (using the ${}_N\{v\}_n^A$ notation of Refs. [4(b),4(c)]), plotted for $R=60$ a.u. Alternative notations for this resonance include the group theoretical notation [32,33] $(K,T,)^A=(3,1)^+$ and the molecular-orbital notation [34,35] $(n_\lambda,n_\mu,m)=(0,6,1)$. Figure 12(a) shows a density plot for this state in (r_1,r_2) coordinates while Fig. 12(b) plots the same density in spheroidal coordinates μ and λ. This state appears at a photon energy of ≈ 5.32 eV in the $\sigma(n=4)$ partial cross section [cf. Fig. 11(c)] and is the first member of a series of deep window resonances in that partial cross section which "converge" to the $n=4$ thresholds for $l \geq 1$. One sees clearly the + character of this resonance from the large antinode at $r_1=r_2$ in Fig. 12(a) and $\mu=0$ in Fig. 12(b).

In Fig. 13, we present density plots for the ${}_5\{0\}_6^-$ resonance feature, plotted for $R=80$ a.u. Alternative notations for this resonance are $(K,T)^A=(4,0)^-$ and $(n_\lambda,n_\mu,m)=(0,9,0)$. The (r_1,r_2) plot in Fig. 13(a) shows that this resonance does not quite have a zero node on the $r_1=r_2$ diagonal line. This may explain why this resonance has such a broad width in the $\sigma(n=4)$ partial cross section [cf. Fig. 11(c) near $\hbar\omega=5.35$ eV]. Using a different set of values for the contours, we see what appears to be a node for $\mu=0$ in the prolate spheroidal coordinate density plot in Fig. 13(b). This confirms the − designation.

In Fig. 14 we present density plots for the very weak resonance feature ${}_6\{1\}_6^+$, plotted for $R=90$ a.u. This resonance is located at $\hbar\omega \approx 5.575$ eV in Fig. 11(d), just below the 6*s* threshold. Alternative notations for this resonance are $(K,T)^A=(2,1)^+$ and $(n_\lambda,n_\mu,m)=(1,6,1)$. The main characteristic of this resonance is its node in $\cos\theta_{12}$, which was

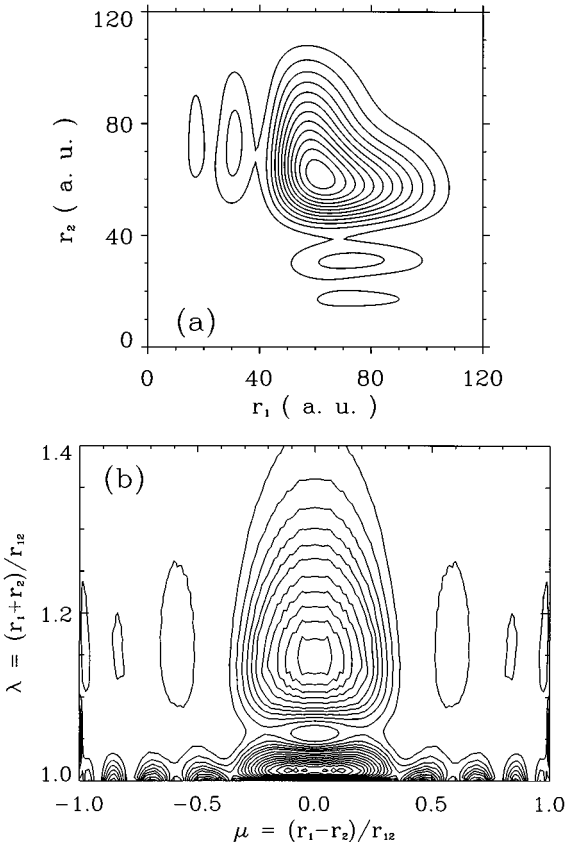

FIG. 14. Doubly excited-state ${}_6\{1\}_6^+$ wave function density plotted at its maximum value in R [i.e., $R\equiv(r_1^2+r_2^2)^{1/2}=90$ a.u.]. (a) Plotted in (r_1,r_2) coordinates. (b) Plotted in prolate spheroidal coordinates (μ,λ). Located near $\hbar\omega=5.575$ eV in Fig. 11(d).

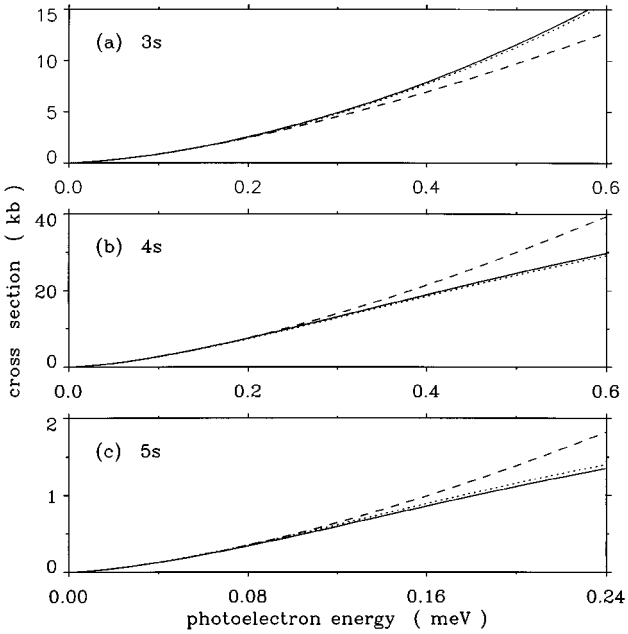

FIG. 15. Partial cross sections $\sigma(ns)$ in dipole velocity (length) approximation [indicated by the solid (dotted) curves] as functions of photoelectron energy E over the first fraction of 1 meV above threshold. The dashed curves are proportional to the Wigner threshold law (i.e., $\propto E^{3/2}$). (a) $\sigma(3s)$. (b) $\sigma(4s)$. (c) $\sigma(5s)$.

clearly visible in our hyperspherical coordinate density plot [6]. The (r_1,r_2) density plot in Fig. 14(a) does not show features in $\theta_{12}=\cos^{-1}(\hat{\mathbf{r}}_1\cdot\hat{\mathbf{r}}_2)$. What we observe from this plot is the + character of this resonance, exhibited by the large antinode for $r_1=r_2$ in Fig. 14(a). This is also a main feature of the prolate spheroidal density plot in Fig. 14(b) for $\mu=0$. We see in the latter, however, the vibrational node in the μ coordinate, corresponding to the θ_{12} node in hyperspherical coordinates [6].

F. Behavior near detachment thresholds

Figure 15 displays the Li ns partial cross sections, for $n=3-5$, on fine energy scales very close to their respective thresholds. Each of these processes involves a single escaping p-wave electron near threshold, which implies a Wigner-type threshold behavior $\sigma(ns)\propto(E-E_{\rm th})^{l+\frac{1}{2}}$ with $l=1$ [36]. Similarly, in the absence of long-range interactions, the $\sigma(np)$ partial cross sections are expected to vary as $\sigma\propto(E=E_{\rm th})^{l_{\rm min}+\frac{1}{2}}$ with $l_{\rm min}=0$ since s-wave ejection dominates near threshold [36]. The Wigner threshold law was tested by Slater *et al.* [37] in the similar context of Cs^- photodetachment near the $Cs(6p\frac{1}{2},6p\frac{3}{2})$ thresholds. In that study, the Wigner law was shown to apply, but only to a remarkably small energy range of $\Delta E=1$ meV above threshold. Calculations for K^- photodetachment [38–40] and for Cs^- photodetachment [41] determined that the unusually small range of validity of the Wigner law stems from the huge dipole polarizability [e.g., α (Cs $6p$) $\approx$ 1000 a.u.] of the excited atomic states. (One typically expects the Wigner law to hold over an energy range $\Delta E\ll r_0^{-2}$ a.u., where r_0 is the range of the electron-atom interaction in the relevant channel.)

In Li^- photodetachment, the Li(nl) dipole polarizabilities for the lower states ($n<3$) are comparable to those of Cs, while for the higher thresholds $n\geq 3$ the polarizabilities are much larger in Li than for Cs $6p$ because they increase roughly as ν_{nl}^7 as the effective quantum number ν of the atomic state nl increases. (This scaling can be understood from the second order perturbation theory expression for the polarizability, and the fact that dipole moments scale as n^2 while the energy denominators scale as n^{-3}.) On the energy scales depicted in Figs. 2, 6, and 8, we do not expect the Wigner law to be very useful for understanding the threshold cross section behavior. The greatly expanded energy scale of Fig. 15, however, shows that the photodetachment cross sections right at the ns thresholds appear to be consistent with the Wigner law.

The ns levels of Li, with quantum defects near $\mu_s=0.4$, are well separated in energy from the energies of hydrogen. However, the Li(nl) quantum defects for $l\geq 1$ are so small ($|\mu_l|\leq 0.04$) that it is reasonable to regard them as hydrogenic to a first approximation. Their degeneracy allows them to mix under the influence of any small interaction. Consequently any Li hydrogenic manifold with principal quantum number $n\geq 3$ forms a quasipermanent dipole moment under the influence of the outermost Li^- electron. The threshold behavior associated with an electron detached into a *perma-*

nent dipole potential $V \rightarrow -a/2r^2$ differs profoundly from that of an electron detached into any shorter-ranged potential such as an *induced* dipole potential $-\alpha/2r^4$. For instance, a shorter-ranged potential must have a *finite* number of resonances (or none) in any channel just below its threshold. An attractive dipole potential is guaranteed to have an *infinite* number of such resonances [11]. Also, the partial cross section for production of a nondegenerate Li(ns) state rises continuously from its zero value at threshold; the analogous cross section for production of a degenerate Li(nl) state, however, rises discontinuously to a finite value at threshold in any channel of the attractive dipole type (i.e., with $a > \frac{1}{4}$). The $4p$, $4d$, and $4f$ partial cross sections in Fig. 7 display abrupt rises at their threshold(s) that look on this energy scale like true discontinuities.

IV. SUMMARY AND CONCLUSIONS

We have presented detailed theoretical results for the partial cross sections resulting from Li^- photodetachment over the energy region from the vicinity of the Li $3s$ threshold to the Li $6s$ threshold (i.e., for 3.8 eV $\leqslant \hbar\omega \leqslant$ 5.65 eV). In the vicinity of the Li $3s$ and $3p$ thresholds our results are in excellent agreement with recent experimental measurements [9]. Above the Li $3p$ threshold, there are as yet no experimental measurements. Throughout this paper we have discussed the role of highly excited two-electron resonances on the predicted photodetachment partial cross sections. We have shown also how the partial cross sections for Li^- photodetachment plus excitation, i.e., $Li^- + \gamma \rightarrow Li\, nl + e^-$, become increasingly similar to those for H^- as the level of excitation n of the residual atom increases. Indeed, we have shown that there is only a limited range of values for n (for Li^-, primarily between the $4s$ threshold and the $5p$ threshold) in which the nonhydrogenic nature of the Li^+ core leads to prominence of doubly excited resonances which are essentially absent in higher-energy regions as well as in H^- photodetachment spectra (due to photodetachment propensity rules for three-body Coulomb systems). We emphasize that this most interesting region for Li^- photodetachment is as yet experimentally unexplored.

We thank D. Hanstorp, E. Lindroth, and D. J. Pegg for providing us with their results prior to publication. This work was supported in part by the U.S. Department of Energy, Division of Chemical Sciences, Office of Basic Energy Sciences under Grant No. DE-FG02-88ER13955 at the University of Nebraska and Grant No. DE-FG02-90ER14145 at the University of Colorado.

[1] P.G. Harris, H.C. Bryant, A.H. Mohagheghi, R.A. Reeder, H. Sharifian, C.Y. Tang, H. Tootoonchi, J.B. Donahue, C.R. Quick, D.C. Rislove, W.W. Smith, and J.E. Stewart, Phys. Rev. Lett. **65**, 309 (1990).

[2] M. Domke, C. Xue, A. Puschmann, T. Mandel, E. Hudson, D.A. Shirley, G. Kaindle, C.H. Greene, H.R. Sadeghpour, and H. Petersen, Phys. Rev. Lett. **66**, 1306 (1991).

[3] J.M. Rost and J.S. Briggs, J. Phys. B **23**, L339 (1990); J.M. Rost, J.S. Briggs, and J.M. Feagin, Phys. Rev. Lett. **66**, 1642 (1991).

[4] (a) H.R. Sadeghpour and C.H. Greene, Phys. Rev. Lett. **65**, 313 (1990); (b) H.R. Sadeghpour, Phys. Rev. A **43**, 5821 (1991); (c) H.R. Sadeghpour, C.H. Greene, and M. Cavagnero, *ibid.* **45**, 1587 (1992); (d) H.R. Sadeghpour and M. Cavagnero, J. Phys. B. **26**, L271 (1993).

[5] J.Z. Tang, S. Watanabe, M. Matsuzawa, and C.D. Lin, Phys. Rev. Lett. **69**, 1633 (1992).

[6] C. Pan, A.F. Starace, and C.H. Greene, J. Phys. B **27**, L137 (1994).

[7] U. Fano and C.M. Lee, Phys. Rev. Lett. **31**, 1573 (1973).

[8] P.F. O'Mahony and C.H. Greene, Phys. Rev. A **31**, 250 (1985); C.H. Greene and L. Kim, *ibid.* **36**, 2706 (1987); C.H. Greene, in *Fundamental Processes of Atomic Dynamics*, edited by J.S. Briggs, H. Kleinpoppen, and H.O. Lutz (Plenum, New York, 1988), pp. 105–127.

[9] U. Berzinsh, G. Haeffler, D. Hanstorp, A. Klinkmüller, E. Lindroth, U. Ljungblad, and D.J. Pegg, Phys. Rev. Lett. **74**, 4795 (1995).

[10] M.J. Seaton, Proc. Phys. Soc. London **77**, 174 (1961).

[11] M. Gailitis and R. Damburg, Proc. Phys. Soc. London **82**, 192 (1963).

[12] F. Robicheaux and C.H. Greene, Phys. Rev. A **46**, 3821 (1992).

[13] W.R. Johnson, D. Kolb, and K.-N. Huang, At. Data Nucl. Data Tables **28**, 333 (1983).

[14] C.E. Moore, *Atomic Energy Levels*, Natl. Bur. Stand. (U.S.) No. NSRDS-NBS35 (U.S. G.P.O., Washington, DC, 1971).

[15] K. Smith, *The Calculation of Atomic Collision Processes* (Wiley, New York, 1971), Sec. 2.4.1.

[16] Anthony F. Starace, in *Handbuch der Physik, Vol. 31: Corpuscles and Radiation in Matter*, edited by W. Mehlhorn (Springer, Berlin, 1982), Sec. 6.

[17] A. Burgess, Proc. Phys. Soc. London **81**, 442 (1963).

[18] M.J. Seaton, Comput. Phys. Commun. **32**, 115 (1984).

[19] C.F. Fischer, *The Hartree-Fock Method for Atoms* (Wiley, New York, 1977).

[20] A.C. Allison, J. Comput. Phys. **6**, 378 (1970).

[21] E. Lindroth, Phys. Rev. A **52**, 2737 (1995); and private communication.

[22] C. Pan, N.Y. Du, A.F. Starace, and C.H. Greene, Bull. Am. Phys. Soc. **38**, 1124 (1993).

[23] M.E. Hamm, R.W. Hamm, J. Donahue, P.A.M. Gram, J.C. Pratt, M.A. Yates, R.D. Bolton, D.A. Clarke, H.C. Bryant, C.A. Frost, and W.W. Smith, Phys. Rev. Lett. **43**, 1715 (1979).

[24] L.A. Morgan, M.R.C. McDowell, and J. Callaway, J. Phys. B **10**, 3297 (1972).

[25] R.S. Oberoi, J. Phys. B **5**, 1120 (1972).

[26] K.T. Chung, Phys. Rev. A **6**, 1809 (1972).

[27] C.D. Lin, Phys. Rev. Lett. **35**, 1150 (1975).

[28] A.C. Fung and J.J. Matese, Phys. Rev. A **5**, 22 (1972).

[29] R.F. Stewart, C. Laughlin, and G.A. Victor, Chem. Phys. Lett. **29**, 353 (1974).

[30] C.D. Lin, J. Phys. B **16**, 723 (1983).

[31] (a) U. Fano, Phys. Rev. **124**, 1866 (1961); (b) A.F. Starace, Phys. Rev. A **16**, 231 (1977).

[32] D.R. Herrick, Phys. Rev. A **12**, 413 (1975); Adv. Chem. Phys. **52**, 1 (1983).
[33] C.D. Lin, Phys. Rev. A **29**, 1019 (1984); Adv. At. Mol. Phys. **22**, 77 (1986).
[34] J.M. Feagin and J.S. Briggs, Phys. Rev. Lett. **57**, 984 (1986); Phys. Rev. A **37**, 4599 (1988).
[35] J.M. Rost, R. Gersbacher, K. Richter, J.S. Briggs, and D. Wintgen, J. Phys. B **24**, 2455 (1991).
[36] See, e.g., U. Fano and A.R.P. Rau, *Atomic Collisions and Spectra* (Academic, New York, 1986), pp. 76 and 77.
[37] J. Slater, F.H. Read, S.E. Novick, and W.C. Lineberger, Phys. Rev. A **17**, 201 (1978).
[38] S. Watanabe and C.H. Greene, Phys. Rev. A **22**, 158 (1980).
[39] K.T. Taylor and D.W. Norcross, Phys. Rev. A **34**, 3878 (1986).
[40] S. Watanabe, J. Phys. B **19**, 1577 (1986).
[41] C.H. Greene, Phys. Rev. A **42**, 1405 (1990).